Journal of Materials Chemistry A

PAPER

View Article Online
View Journal | View Issue

Cite this: J. Mater. Chem. A, 2015, 3, 10526

Hierarchical i–p and i–n porous heterojunction in planar perovskite solar cells†

Hsueh-Chung Liao,[ab] Cheng-Si Tsao,*[c] Meng-Huan Jao,[a] Jing-Jong Shyue,[d] Che-Pu Hsu,[a] Yu-Ching Huang,[c] Kuo-Yo Tian,[a] Charn-Yin Chen,[c] Chun-Jen Su[e] and Wei-Fang Su*[a]

Received 25th March 2015
Accepted 2nd April 2015

DOI: 10.1039/c5ta02184g

www.rsc.org/MaterialsA

A hierarchical pore network in planar $CH_3NH_3PbI_3$ perovskite is demonstrated herein. Quantitative characterizations by grazing incidence small angle X-ray scattering (GISAXS) with modeling and complementary microscopic observations provide insight at various length scales. It is a pore structure comprised of nano-scaled primary pores aggregating into meso-scaled fractal networks within the perovskite layer. Its structural evolution and mechanistic interpretation are explored with respect to different preparation methods/steps. The time-of-flight secondary ion mass spectrometer (TOF-SIMS) results suggest the infiltration of hole transporting materials (HTM) or electron transporting materials (ETM) deposited on top at different length scales. The inter-penetrating perovskite/HTM or perovskite/ETM form i–p or i–n one-sided porous heterojunctions, respectively, over the typically regarded planar-stacked heterojunction. They show distinctive photovoltaic characteristics and behaviors in which the large i–n interfaces at the nanoscale lead to highly efficient, hysteresis-free and reliable solar cell devices. The morphology–performance correlation is helpful for associated design of device architecture and processing toward higher efficiency and stability.

Introduction

Organic/inorganic hybrid perovskite solar cells have attracted considerable attention in the past few years due to their high performance and advantages of low cost, solution processability, light weight, flexibility, *etc.*[1–17] As compared to the current power conversion efficiencies (PCEs) of other emerging photovoltaic (PV) systems (*e.g.* organic PV ~10% and dye-sensitized solar cells (DSSCs) ~12%, respectively),[3,18,19] perovskite solar cells show exciting progress with PCE up to 19.3% (generally over 15%)[2,4,6,9,10] in academic publications and beyond 20% in the most recently reported efficiency chart.[20] In the development of perovskite solar cells, two types of device structure are typically employed (1) meso-structured solar cell (MSSC) with metal-oxide serving as the template scaffold for the infiltration of perovskite absorber,[2,5,7,8,11,21,22] (2) p–i–n planar heterojunction (PHJ) with perovskite thin film sandwiched between p- and n-type charge collecting layers. Recently, the PHJ solar cells have delivered high PCE values >15% by integrating perovskite films in either the forward structure[23–30] or inverted structure,[4,6,31–34] in which the former device collects electrons and holes by metal electrode and transparent electrode, respectively, and the latter device does the opposite. These significant progresses show that the perovskite absorber can function at high efficiency in simplified device architectures, favorable fabrication control, and thus move toward the goal of commercialization.

The methylammonium lead halide ($CH_3NH_3PbX_3$) represents one of the most efficient hybrid perovskite materials. It is reasonable that the mix halide with chloride doping ($CH_3NH_3PbCl_xI_{(3-x)}$) shows high efficiency in the PHJ structure, owing to its long carrier/exciton diffusion length up to 1 μm, which exceeds film thickness of around ~300 nm.[26,31,33,35–37] In contrast, for the triiodide perovskite $CH_3NH_3PbI_3$, a shorter carrier/exciton diffusion length (~100 nm)[36] was reported with an order of magnitude higher bimolecular recombination rate than the mixed-halide system.[36,37] However, high efficiencies of PHJ solar cell with triiodide perovskite have been achieved, either in the forward or inverted device structure.[6,23–25,27–29,32,34] It

[a]Department of Materials Science and Engineering, National Taiwan University, No. 1, Sec. 4, Roosevelt Road, Taipei 10617, Taiwan. E-mail: suwf@ntu.edu.tw; Fax: +886 2 33664078; Tel: +886 2 33664078
[b]FrontMaterials Co. Ltd., No. 2-3, Ln. 66, Zhulin Rd., Yonghe Dist., New Taipei City 23441, Taiwan
[c]Institute of Nuclear Energy Research, No. 1000, Wenhua Road, Longtan Township, Taoyuan County 32546, Taiwan. E-mail: cstsao@iner.gov.tw; Tel: +886 3 4711400 ext. 3420
[d]Academia Sinica, No. 128, Academia Road, Section 2, Nankang, Taipei 115, Taiwan
[e]National Synchrotron Radiation Research Center, No. 101, Hsin-An Road, Hsinchu 300-77, Taiwan

† Electronic supplementary information (ESI) available: Effect of substrate on the GISAXS experiments; interface (surface) area determined by Porod's law. GISAXS profiles of two-step processing of PbI_2 layer (step I) and perovskite layer. 1D XRD pattern of PbI_2 and two-step processed perovskite. See DOI: 10.1039/c5ta02184g

was reported that the processing strategies significantly affect the device performances.[6,25,32,34] Therefore, it can be speculated that there exists a critical structure governing the mechanism and thus the device characteristics.

Additionally, to our knowledge the inverted PHJ solar cell using ETL (*e.g.* TiO_2) as substrates is under debate in the perovskite research community, owing to the notorious photocurrent hysteresis and mismatch of photocurrent obtained between current–voltage scanning and the external quantum efficiency spectrum.[38–41] In contrast, such issues are found to be less significant in the forward PHJ solar cell using HTM as substrates but with similar solution-processed perovskite.[24,25,27–30,34] The morphology of the perovskite layer and its stacking with the ETL and HTL layer should play a critical role in achieving such different photovoltaic characteristics. However, the correlations among processing, morphologies and photovoltaic performances are still not clear. To date, the structural information of perovskite obtained from scanning electron microscopy (SEM) focusses on the surface topography, coverage and/or roughness, which are very limited to mechanistic understanding. In this work, we utilized grazing-incidence small-angle scattering (GISAXS) technique[42–44] as an effective tool to quantitatively probe the nanostructures of the $CH_3NH_3PbI_3$ perovskite layer at various length scales. A hierarchical pore structure within the perovskite layer is reported herein over the current structural observations. We present the existence and characterization details of nano-scaled pore structures and networks in complement with microscopic observations. Their evolution in different preparation methods/steps is explored with mechanistic interpretation. The TOF-SIMS was performed to depth mapping and profiling the infiltration of HTM (inverted structure) or ETL (forward structure). They respectively form an i–p or i–n porous one-side heterojunction over the traditionally regarded planar-stacked heterojunction. We correlate the device performances and device behavior to such a porous heterojunction, which show distinctive photovoltaic behavior between the forward (i–n) and inverted (i–p) PHJ solar cell. The results address the issues of both photocurrent hysteresis and photocurrent, helping the further design of highly efficient and highly stable perovskite solar cells.

Results and discussion

In this work, we fabricated two types of layer-by-layer solar cells, *i.e.* forward structure and inverted structure, and their configurations are shown in Fig. 1a and b, respectively. For the forward structure, poly(3,4-ethylenedioxythiophene)polystyrene sulfonate (PEDOT:PSS) and phenyl-C_{61}-butyric acid methyl ester ($PC_{61}BM$) were selected as HTM and ETM, respectively, while in the inverted structure the perovskite layer is sandwiched between TiO_2 (ETM) and 2,2′,7,7′-tetrakis-(*N*,*N*-di-4-methoxyphenylamino)-9,9′-pirobifluorene (spiro-OMeTAD, HTM). For the processing of perovskite $CH_3NH_3PbI_3$, there are generally two methods. (1) One-step method: two precursors lead iodide (PbI_2) and methylammonium iodide (CH_3NH_3I) are mixed and then spin-coated on substrates, followed by thermal treatment.[5,7,45,46] (2) Two-step method (also called sequential deposition): a PbI_2 layer is first deposited by spin-coating (step I), which subsequently forms $CH_3NH_3PbI_3$ perovskite crystallites by reacting with CH_3NH_3I solution *via* spin coating or immersion (step II).[2,6,23–25,27] Generally, in PHJ solar cell the two-step method leads to remarkably higher PCE. Fig. 1c and d plot the current density–voltage (*J*–*V*) curves of the forward and inverted PHJ solar cells, respectively, which formed with one-step and two-step processed perovskite, respectively. The devices are scanned in either the positive direction (V_{oc}–J_{sc}) or the negative direction (J_{sc}–V_{oc}), where the J_{sc} and V_{oc} denote short circuit current density and open circuit voltage, respectively. Their photovoltaic characteristics are summarized in Table 1 with statistics. Note that for one-step processed perovskite in the forward structure, parts of the devices are short without photovoltage, hence their statistics are not included.

According to Table 1, the two-step processed device exhibits remarkably higher PCE than one-step processing in both device architectures. In comparison between two different device structures, the inverted one (Fig. 1d) shows significance differences between positive-scanned and negative-scanned curves while this effect (*i.e.* hysteresis effect) is subtle in the forward one. Furthermore, for the forward structure the integrated current density from the EQE spectrum ($\sim$17.0 mA cm^{-2}) plotted in Fig. 1e is consistent with the value obtained from *J*–*V* scanning (Fig. 1c, 17.7 mA cm^{-2}); in contrast, in the inverted structure the EQE-integrated current density ($\sim$15.0 mA cm^{-2}) is much lower than that extracted from *J*–*V* scanning ($\sim$19–20 mA cm^{-2}). Such inconsistency is typically observed in the inverted PHJ solar cell using TiO_2 planar substrates.[31,38] In the literature, researchers either normalized their EQE[31] or preconditioned their devices by inputting a forward bias under light soaking before EQE measurement.[38,47] However, such treatment is controversial for accurately evaluating the device performance for practical applications. We performed the photocurrent and photovoltage tracing with turning on and turning off the light as shown in Fig. 2f and g. Both device structures show an instant response to turning the light on and off. In the forward device the J_{sc} ($\sim$17 mA cm^{-2} V^{-1}) and V_{oc} ($\sim$0.95 V) are steady during light-on and match the values obtained from *J*–*V* scanning (Fig. 1c and Table 1), whereas in the inverted structure both characters decay during light soaking. Specifically, the J_{sc} value read in Fig. 1d for the inverted structure is nearly identical only to the first point of the photocurrent trace (Fig. 1f), which then decays and stabilizes to one-third ($\sim$7 mA cm^{-2}) of the initial value after being illuminated for 300 s. This value could be the real J_{sc} for the inverted PHJ solar cell being practically used, since it attains a stable output. It is of great interest that for MSSC with the same underlying materials, TiO_2, but with perovskite/TiO_2 intermixing on the nanoscale, such a device architecture is generally hysteresis-free and exhibits a reliable photocurrent.[39,40] The nano- and microstructure (morphology) of the perovskite layer could be critical in accounting for this photovoltaic behavior.

The morphologies of the perovskite thin films prepared by the one-step and two-step methods were investigated by synchrotron GISAXS. Fig. 2a shows the GISAXS profiles, *I*(*Q*), of

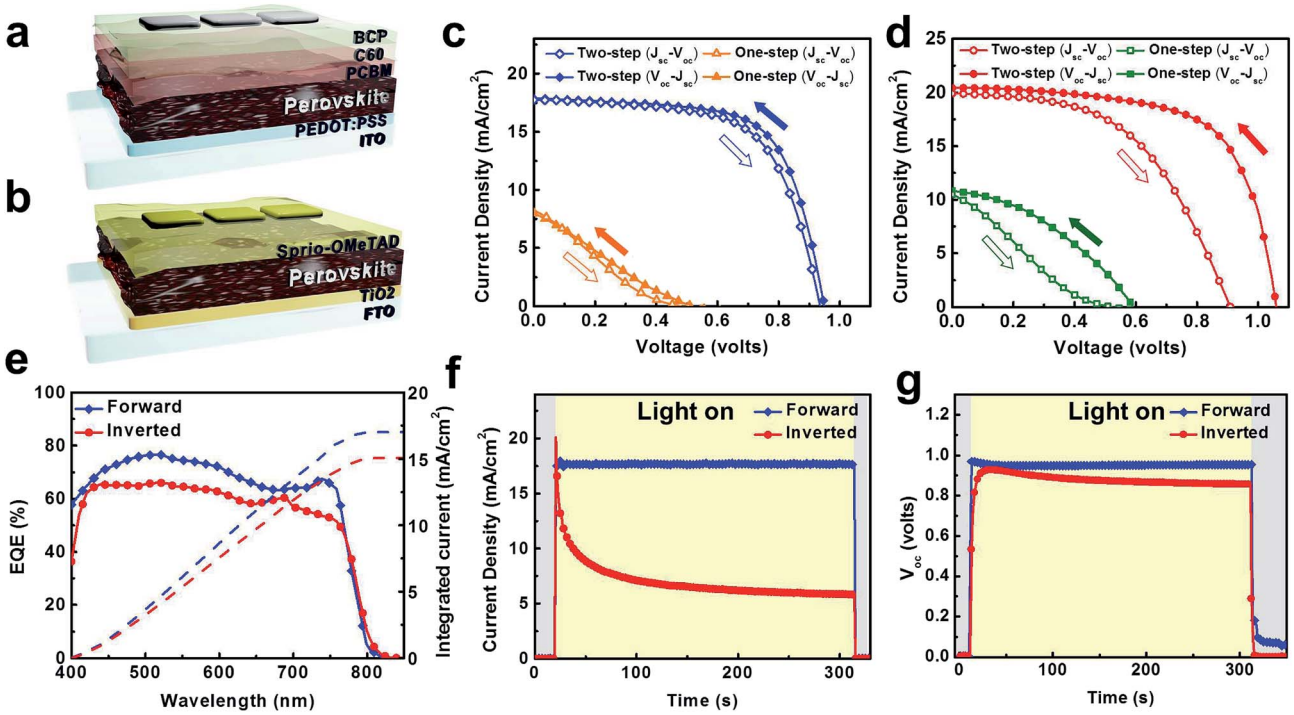

Fig. 1 (a and b) Illustration of PHJ solar cell in the forward (a) and inverted (b) structure. (c and d) *J*–*V* curves of forward (c) and inverted (d) PHJ solar cell using one-step and two-step processed perovskite, respectively. The dependence of scanning direction are also plotted. (e) EQE spectrum and corresponding integrated current density of forward and inverted devices with two-step processed perovskite. Photocurrent (f) and photovoltage (g) response of turning on and turning off the incident light in forward and inverted devices with two-step processed perovskite.

triiodide perovskite film processed by the one-step and two-step methods, respectively. To eliminate the effect of multiple scattering caused by the reflection and refraction beams in the grazing-incidence geometry,[48] the in-plane GISAXS profiles taken from the Yoneda peak in the measured 2D GISAXS pattern (red marked region in Fig. 2a inset) can be analyzed using the conventional SAXS model.[48–50] The GISAXS profiles in this study are represented by this kind of in-plane GISAXS profile. In Fig. 2a the GISAXS profiles exhibit the behavior of power-law scattering ($I(Q) \propto Q^{\alpha}$; $2.1 \leq \alpha \leq 2.6$) in the middle Q range (0.007–0.3 Å^{-1}). The exponent value, α, reveals the typical characteristic of mass fractal. The model that can give the best fit needs to include the structure factor of the fractal network comprised of the primary particles (pores in this case). Specifically, the GISAXS intensities are mainly contributed to from the morphology of the fractal network structure, which is formed by the aggregation of primary pores (at multi-length scales). The GISAXS intensity profile can be expressed as eqn (1)

$$I_{SM}(Q) = P(Q)S(Q), \quad (1)$$

Table 1 Photovoltaic characteristics of forward and inverted devices with one-step and two-step processed perovskite, respectively. The values in parentheses show the average PCEs and PCE distribution (standard deviation) obtained from 15 devices made from 5 independently prepared BHJ films

Device structure	Preparation method	Scan direction	V_{oc} (V)	J_{sc} (mA cm^{-2})	FF (%)	PCE (%)
Forward	One-step	J_{sc}–V_{oc}	0.51	8.1	23.5	0.97[a]
		V_{oc}–J_{sc}	0.48	7.8	20.1	0.75[a]
	Two-step	J_{sc}–V_{oc}	0.93	17.7	63.0	10.4 (9.6 ± 1.0)
		V_{oc}–J_{sc}	0.95	17.7	66.0	11.1 (9.9 ± 0.9)
Inverted	One-step	J_{sc}–V_{oc}	0.59	10.9	44.9	2.9 (2.2 ± 1.2)
		V_{oc}–J_{sc}	0.50	10.5	20.2	1.1 (0.6 ± 0.4)
	Two-step	J_{sc}–V_{oc}	0.90	19.9	50.5	9.0 (7.3 ± 1.1)
		V_{oc}–J_{sc}	1.06	20.4	65.3	14.1 (13.6 ± 0.9)

[a] Parts of the devices are short without photo-voltage, hence their average and standard deviation of PCEs values are not presented.

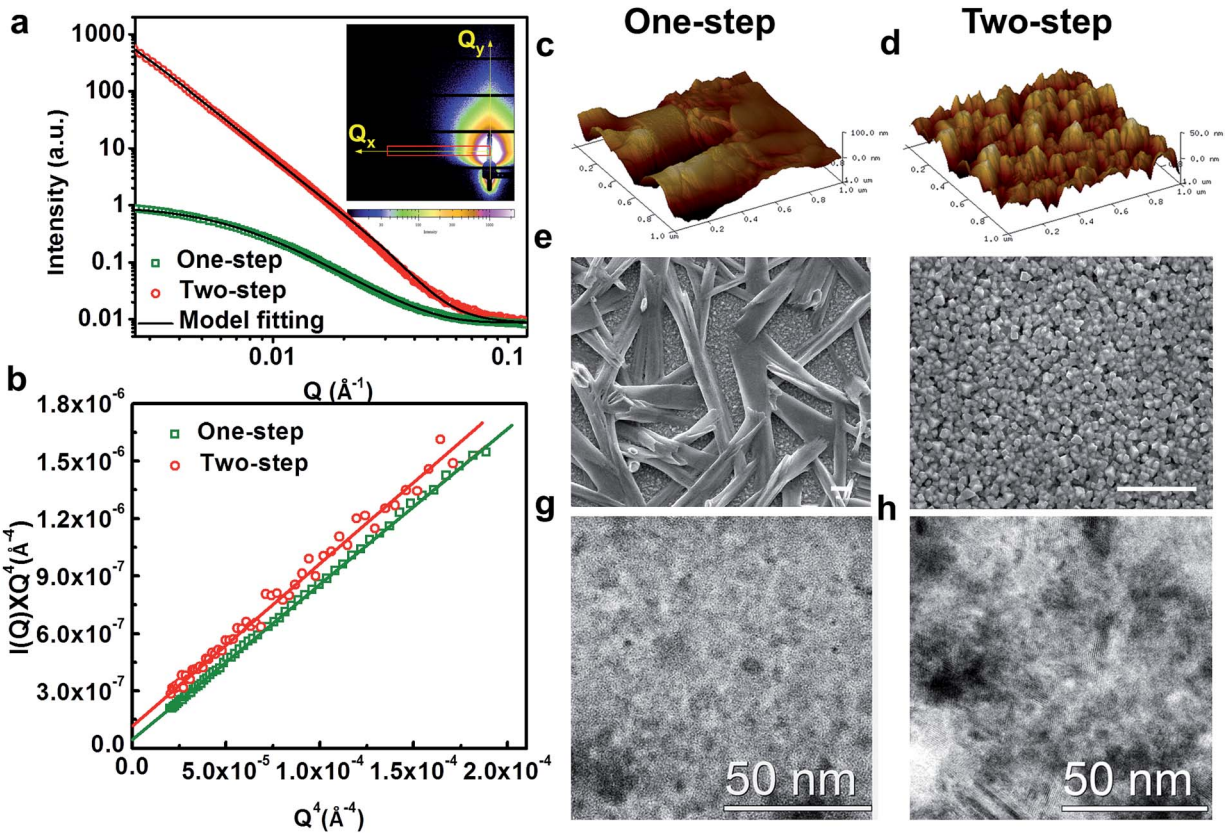

Fig. 2 Morphological characterization of one-step and two-step processed perovskite. (a) GISAXS profiles of perovskite layers prepared by one-step and two-step processing methods, respectively. The inset shows the 2-D GISAXS pattern of the two-step processed perovskite with the marked region (red) reduced to the 1D GISAXS profile accordingly. They can be fitted by the model calculation (solid lines). (b) Plots of $Q^4I(Q)$ *vs.* Q^4 from GISAXS profiles of the one-step and two-step processed perovskite layer, respectively. (c and d) AFM images, (e and f) SEM images and (d and f) HRTEM images of the one-step and two-step processed perovskite, respectively. The scale bars in the SEM images are 1 μm in length.

where $P(Q)$ is the form factor of spherical pores as the primary unit. $S(Q)$ is the fractal structure factor, describing the interaction between primary pores in this fractal-like aggregation system. $P(Q)$ includes a pre-factor, which is the product of pore volume fraction φ and the square of scattering length density contrast between pore and matrix. $S(Q)$ is given by eqn (2)[51]

$$S(Q) = 1 + \frac{\sin[(D-1)\tan^{-1}(Q\xi)]}{(QR_{SM})^D} \frac{D\Gamma(D-1)}{\left[1+1/(Q\xi)^2\right]^{(D-1)/2}}, \quad (2)$$

where ξ is the characteristic length of the fractal-like network domain (formed by the aggregation of the primary pores). D is the fractal dimension. The least-squares fitting calculation of eqn (1) considers the polydispersity, p, of primary pores having a Schulz size distribution with mean radius R. Note that the volume fraction values, φ, determined herein are only for relative comparison rather than the absolute values, because the absolute scattering contrast values cannot be measured in the grazing angle configuration. The domain size of the fractal network can be approximately characterized by the Guinier radius (*i.e.* radius of gyration: $R_g = [D(D+1)/2]^{1/2}\xi$).[52] The obtained structural parameters are summarized in Table 2. The substrate used for the GISAXS experiments was Si. The substrate effect on the morphology is discussed in the ESI, Fig. S1†).

According to the structure parameters in Table 2, for the one-step case the difference between the fitted ξ value is not large enough to be comparable to the other fractal cases. A potential uncertainty from the limitation of the SAXS model may exist to the realistic fractal system. The cut-off function as the basis of the structure factor we used is the most used exponential cutoff.[53] The total interface area (including the surface area) of such a fractal pore network can be determined by the Porod law,[54] according to GISAXS profiles in the high Q region as shown in Fig. 2b (details including subtraction of the background are shown in the ESI†).

Within the planar perovskite thin-film prepared by a one-step method (*cf.* Table 2), there exists a pore structure comprised of polydispersed primary pores of mean radius

Table 2 Structural parameters (extracted from the model fitting to GISAXS profiles) of the hierarchical pore structure in the one-step and two-step processed perovskite

Preparation method	Rel φ (%)	R (nm)	D	ξ (nm)	R_g (nm)
One-step	9	3.6	2.33	14	28
Two-step	37	5.1	2.80	120	280

3.6 nm. The primary pores aggregate into a fractal network with fractal dimension 2.33 and domain size ($2R_g$) ~55.6 nm. The previous studies focusing on the one-step method pointed out that severe de-wetting or agglomeration occurs during perovskite crystallization on ETM.[2] It is consistently observed in our work, as shown in Fig. 2c and e of the atomic force microscope (AFM) image and SEM image, respectively. The de-wetting feature results in incomplete coverage of perovskite with gaps between strip-like grains (μm scale in width, Fig. 2c and e). The micro-scaled gaps can be regarded as defects because they lead to direct contact between HTM and ETM and thus cause the device performance to deteriorate. In contrast, the pore structures within the grains discovered in this study can accommodate the infiltrated ETM (forward structure) or HTM (inverted structure), increasing the p–i (HTM/perovskite) and n–i (ETM/perovskite) interfacial area, respectively (discuss later). The HRTEM image shown in Fig. 2g provides the complementary observations into the strip-like grains in real space. It clearly reveals the existence of such a pore structure (light color) with inter-connection into pore channels.

Regarding the perovskite film prepared by a two-step method, the AFM (Fig. 2d) and SEM images (Fig. 2f) reveal distinctive meso-scale morphology as compared to the one-step processed perovskite. It can be clearly observed that the film is comprised of ~100 nm grains, which continuously pack and cover the substrates. The meso-scale morphology is consistent with the previous observations presented by Kelly *et al.*[6] In the present study we moreover provide insights into the nanoscale structure inside the grains with quantitative information. Within the grains, the GISAXS results (Table 2) show a substantially higher relative volume fraction of the pore structure (~37%, pore size ~5.1 nm in radius) than the one-step film. Additionally, the fractal dimension (D) and domain size ($2R_g$) of the fractal network increase to 2.80 and 560 nm, respectively, implying that the pores connect to the 3D network throughout the perovskite layer (>300 nm of layer thickness) with reduced local pore structure. Moreover, the total interface area (including the surface area) determined by the Porod law[54] (*cf.* Fig. 2b and ESI†) is found to be three times higher in the two-step processed perovskite than in the one-step. The above results suggest that the hierarchical pore structure takes the major nanostructure within the perovskite layer. The TEM observation of the grains shown in Fig. 2h again supports the pore structure. It can be clearly seen that the primary pores (light color) connect to form pore channels, which are surrounded by crystallites (with obvious lattice fringes).

The formation of the pore structure can be attributed to the spatial dispersion of such crystallites within the ~100 nm grains (discuss later). The TOF-SIMS imaging and depth profiling by *in situ* ion sputtering were utilized to examine if the hierarchical pore structure is open to accommodate the infiltrated HTM or ETM, which is deposited on top of the perovskite layer in the inverted and forward structure, respectively. Regarding the inverted device structure, the Pb and $CH_3OC_6H_4NCH_3$ were chosen as the fragments for perovskite and HTM spiro-OMeTAD, respectively. Fig. 3 shows the intensity mapping and depth profiling of the Pb and $CH_3OC_6H_4NCH_3$ fragments for both one-step and two-step processed perovskite, respectively. $CH_3OC_6H_4NCH_3$ is representative of the fragment from spiro-OMeTAD. Note that the images are on an anisotropic scale, *i.e.* 50 μm along the horizontal direction and *ca.* 70–100 nm (according to the sputtering rate *ca.* 0.1 nm s^{-1}) along the vertical direction. For the one-step processed perovskite, the strip-like grains and gaps (in micro-scale) are clearly seen in the Pb fragment mapping (blue). However, such micro-scaled structures are not observed in the $CH_3OC_6H_4NCH_3$ fragment mapping (green). Instead, it reveals nanostructures within the perovskite. The results indicate that the HTM penetrates into the perovskite not only through the micro-scaled gaps but also through the pore structures within the micro-scaled grains. The similar nanostructures are also found in the $CH_3OC_6H_4NCH_3$ fragment mapping of the two-step processed sample. Distinctively, its depth profile shows a remarkable hump of $CH_3OC_6H_4NCH_3$ intensity, implying that a larger amount of HTM infiltrates into the perovskite as compared to the one-step processed perovskite. In such a two-step case, possible infiltration pathways include the pore structures within the grains or the grain boundaries, as recently demonstrated by Shao *et al.*[24] It is hard to quantitatively compare the respective amounts, but we deduce that the pore structure could dominate the accommodation. This is because the grain stacking in the two-step processed perovskite (Fig. 2f) is closer than the one-step processed perovskite (Fig. 2e), which shows micro-scaled gaps. However, the former case reveals a larger amount of HTM infiltration (Fig. 2a and b). Furthermore, it is consistent with the quantitative GISAXS results (Table 2) that the volume fraction of the pore structures and total interface area (Fig. 2b and ESI†) are significantly higher in the two-step processed perovskite than in the one-step. The TOF-SIMS results prove that the hierarchical pore structure is open for accommodation of HTM. The similar infiltration through the pore structure and grain boundaries is also observed in the TOF-SIMS mapping and depth profiling (Fig. 3c) of two-step processed perovskite in the forward structure, in which the $PC_{61}BM$ was spin coated on the top of the perovskite layer. The C_6 fragment was used to represent $PC_{61}BM$.

Mechanistic understanding of the formation of the hierarchical pore structure is discussed as follows. We mainly focus on the two-step process owing to the minor role of the pore structure (low volume fraction, Table 2) and significant de-wetting in one-step processed perovskite. The GISAXS profile of the PbI_2 layer (step I of the two-step processing) is plotted in the ESI.† The profile shows a fractal dimension of $\alpha = 3.6 (I(Q) \propto Q^{\alpha}$; $3 \leq \alpha$ (=3.6) ≤ 4), which reveals the characteristic of surface fractal morphology at different scales and little internal pore network. This indicates that the dipping of CH_3NH_3I in step II leads to the transition from surface fractal scattering of PbI_2 to pore mass fractal scattering of perovskite $CH_3NH_3PbI_3$. It can be speculated that the CH_3NH_3I solution diffuses from the surface of the PbI_2 framework into the interior, which enables the crystallization of $CH_3NH_3PbI_3$. The X-ray diffraction (XRD) patterns of the PbI_2 film (step I) and perovskite (step II) (ESI†) suggest the nearly complete transformation after dipping in CH_3NH_3I solution for 40 s. Therefore, the dispersion/

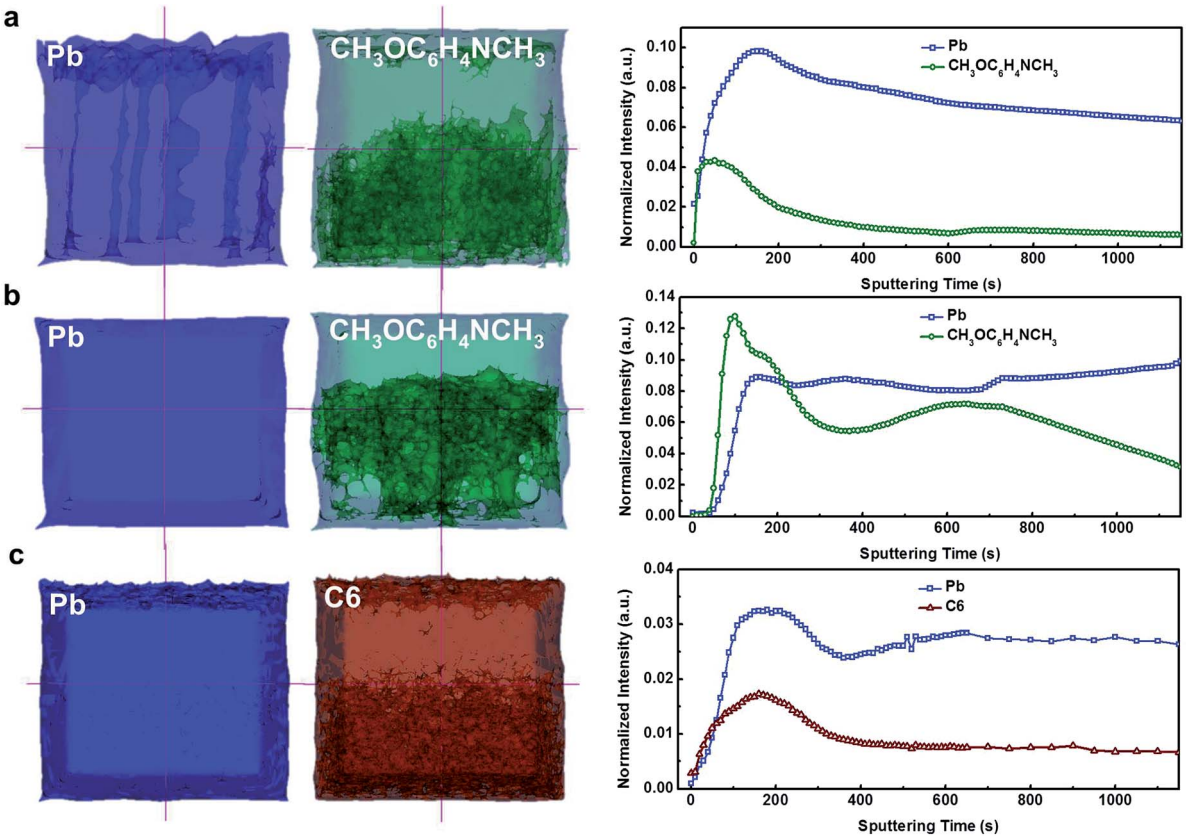

Fig. 3 TOF-SIMS intensity mapping (left images) and depth profiling (right plots) of (a) one-step processed and (b and c) two-step processed perovskite layers with (a and b) HTM spiro-OMeTAD and (c) ETM $PC_{61}BM$ spin coated on top. Pb, $CH_3OC_6H_4NCH_3$ and C_6 were chosen as the representative fragments for perovskite, HTM spiro-OMeTAD, and ETM $PC_{61}BM$, respectively. The scales of the intensity mapping images are 50 μm in width and *ca.* 70–100 nm in depth.

construction of perovskite crystallites within the grains (~100 nm) leaves the fractal pore network and its spatial distribution as likely to extend from the surface entry pores or boundary gaps between the PbI_2 grains, which gradually decreases along the vertical depth direction. This results in a favorable diffusion-like percolation network or porous structure. In conclusion, the PbI_2 film can serve as a framework with a high-contact-area fractal surface structure. Afterwards, an open, penetrating and internal pore network forms during step II for the following HTM or ETM infiltration. According to the quantitative morphological investigations shown above, the 3D and 2D nanostructures of this hierarchical porous perovskite and its associated evolution during two-step processing are illustrated in Fig. 4 at various length scales.

Considering that $CH_3NH_3PbI_3$ is an intrinsic semiconductor, the infiltration of HTM or ETM into the pore structure throughout the perovskite layer forms an i–p or i–n porous heterojunction. This percolation on the nanoscale contributes to the high efficiency of $CH_3NH_3PbI_3$ PHJ, although its exciton/carrier diffusion length (~100 nm) is one-third of the film thickness (~300 nm).[35] Specifically, the intermixing of perovskite/HTM or perovskite/ETM is at different length scales, from primary pores of ~10 nm, grain boundaries of ~tens of nanometers, to pore channels and a network of hundreds of nanometers, which is a typical characteristic of the fractal structure (*i.e.* hierarchical heterojunction). Such an i–p or i–n one-sided junction not only provides a substantial interfacial area for carrier collection, but influences the photovoltaic behavior. It has been recently reported that the $PC_{61}BM$ could successfully passivate the defect density state of perovskite and hence release the hysteresis.[24] We consistently observe in our work that the forward structure shows a hysteresis-free and reliable short-circuit current (Fig. 1), owing to the inter-penetration of $PC_{61}BM$ and perovskite on the nanoscale. Such an i–n (perovskite/$PC_{61}BM$) heterojunction structure is analogous to the MSSC in which the TiO_2 nanoparticles (~20 nm) are inter-mixed with perovskite crystallites on the nanoscale and reveal reliable photovoltaic behavior.[39,40] In contrast, for the inverted PHJ with an i–p one-sided junction, the electron collection only relies on the planar contact between the perovskite layer and the TiO_2 compact layer. Recent work carried out by Edri *et al.* pointed out that in perovskite the diffusion length of the electron is shorter than the hole.[55,56] Highly efficient HTM-free devices can be made, as the perovskite itself is a good hole conductor.[57–61] Therefore, the present work further elucidates why large i–n interfaces are essential to achieve highly efficient, hysteresis-free and reliable perovskite solar cell devices from the morphological point

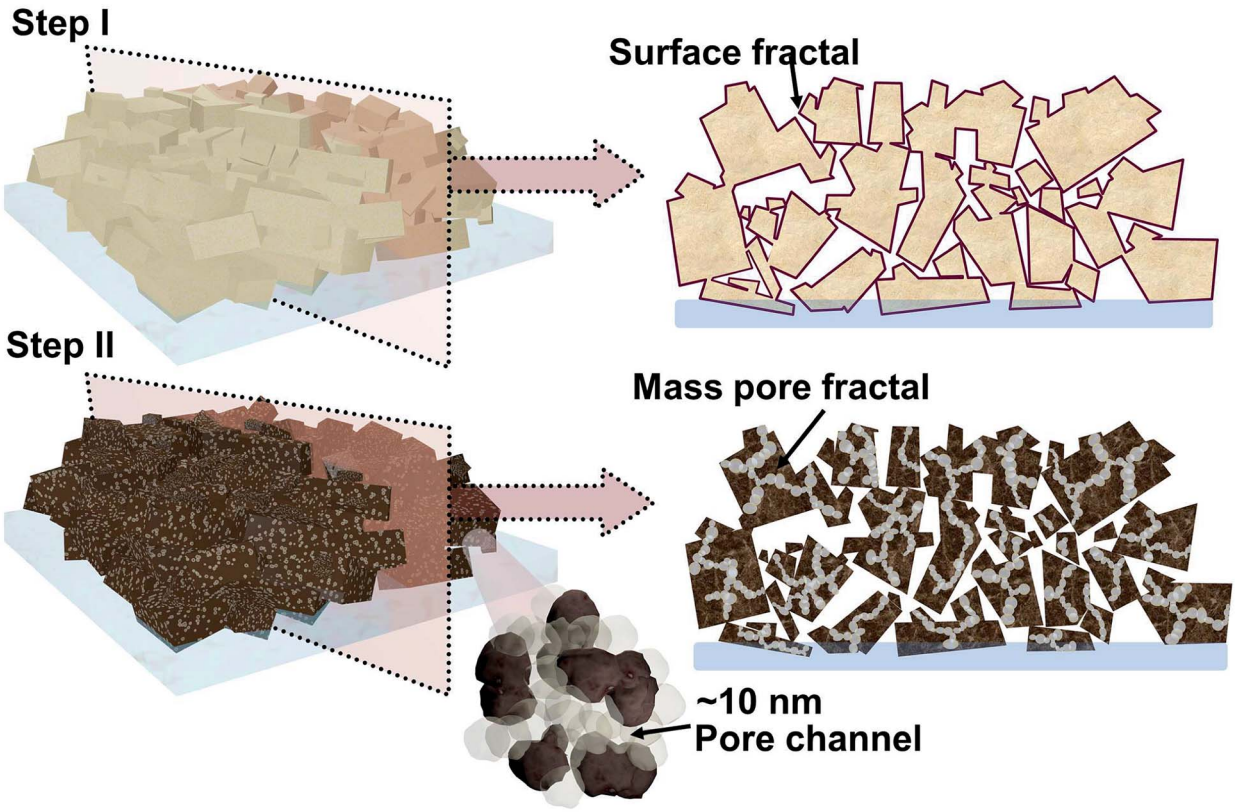

Fig. 4 Schematic illustration of two-step processed perovskite. The PbI_2 layer in step I serves as a framework with surface fractal characteristics. During step II, the porous perovskite layer is formed, which is comprised of nanopores (~10 nm in diameter) interconnecting into pore channels and meso-scaled pore networks among stacked grains (~100 nm).

of view. The i–n porous heterojunction would be the target of ideal design toward high performance in the future.

Conclusions

We demonstrate the hierarchical pore structure at different length scales in PHJ $CH_3NH_3PbI_3$ perovskite solar cells. Its structural information is presented quantitatively, from primary pores to their aggregation into fractal networks at the nano- and meso-scale, by GISAXS analysis with complementary morphological observation including SEM, TEM, AFM, *etc.* The pore structure formed in two-step processed perovskite takes the majority with relatively high volume fraction and large-scale network. The HTM or ETM was found to infiltrate in-depth through such porous structures over different length scales. An i–p (perovskite/HTM) or i–n (perovskite/$PC_{61}BM$) one-sided hierarchical porous heterojunction can be formed, which plays a crucial role in photovoltaic behaviors. Larger i–n interfaces are essential to passivate the hysteresis and stable output photocurrent, and hence attain high efficiency and reliable solar cell performance. The morphological insights and associated mechanistic interpretation and correlation with device performances are presented herein, which informatively guide the rational strategies for further processing of high efficiency perovskite solar cells.

Experimental

Solar cell device fabrication

For the inverted device, the fluorine doped tin oxide (FTO) substrate was ultrasonically cleaned by a series of solvents, DI water, ammonium/deionized water/hydrogen peroxide, methanol, and isopropanol, followed by oxygen plasma treatment for 15 minutes. A TiO_2 sol–gel solution (Catalog no. AA, FrontMaterials. Co. Ltd.) was spin coated on FTO at 1000 rpm for 40 s and sintered at 500 °C for 30 minutes. The obtained FTO/TiO_2 substrate was transferred into a humidity box with relative control of 3% for the following perovskite layer processing. For the one-step processing, PbI_2 (Catalog no. 19886, ACROS) and methylammonium iodide (CH_3NH_3I, Catalog no. BA, FrontMaterials. Co. Ltd.) in a weight ratio of 3 : 1 were dissolved in *N*,*N*-dimethylformamide at a concentration of 40 wt%. The solution was stirred at 50 °C overnight and spin coated on the FTO/TiO_2 substrate at 2000 rpm for 30 s. Subsequently, the perovskite thin film was thermally annealed at 100 °C for 2 minutes. The film color changed from yellow to dark brown during thermal treatment. For the two step processing, PbI_2 (460 mg ml^{-1} in *N*,*N*-dimethylformamide) was first spin coated on a FTO/TiO_2 substrate at 3000 rpm for 15 s, followed by thermal annealing at 70 °C for 10 minutes. The PbI_2 film was then dipped into CH_3NH_3I solution (45 mg ml^{-1} in isopropanol) filled in a petri dish for 40 s. The film color changed from yellow to dark brown

immediately after immersion. The obtained perovskite film was rinsed with isopropanol and dried by N_2 flow and thermally annealed at 100 °C for 2 hours. The hole transporting materials (HTM) Spiro-OMeTAD (Catalog no. EA, FrontMaterials Co. Ltd.) doped with 28.5 μl 4-*tert*butylpyridine and 17.5 μl lithium-bis-(trifluoromethanesulfonyl)imide (Li-TFSI) chlorobenzene (80 mg ml^{-1}) were spin coated at 4000 rpm for 30 s. The Au electrode was then thermally evaporated to finish the solar cell device with an active area of 0.09 cm^2. For the forward structure, PEDOT:PSS (Baytron-P 4083) layer was spin coated on cleaned indium tin oxide (ITO) glass at 6000 rpm for 40 s, followed by thermal annealing at 130 °C for 15 min. The depositions of the perovskite layer for the one-step and two-step processes were identical to the procedures described in the inverted structure. Subsequently, $PC_{61}BM$ (American Dye Source) with a concentration of 20 mg ml^{-1} in chlorobenzene was spin coated on the perovskite layer at 1000 rpm for 40 s. The devices were completed by thermal evaporation C_{60} (20 nm), BCP (8 nm) and Al (100 nm) with an active area of 0.06 cm^2. The devices were tested in air with a shadow mask of 0.12 cm^2 and 0.08 cm^2 for the inverted and forward devices, respectively. The PCEs and photocurrent/photovoltage tracing were characterized under A.M. 1.5 radiation (100 mW cm^{-2}) of a solar simulator source (Newport Inc.) and recorded on a Keithley 2400 source meter.

Morphological characterizations

The GISAXS measurement was performed at beam line 23A of NSRRC, Taiwan. The experimental configuration can be found in our previous work.[42–44] Briefly, the one-step and two-step processed perovskite were spin-coated on Si substrates and Si/TiO_2 substrates, respectively. Note that the processing conditions of the compact TiO_2 film and the perovskite layer were identical to those used in solar cell device fabrication. The monochromated X-ray beam (10 keV, wavelength = 1.24 Å, incidence angle = 0.2°) was used to characterize the sample films. The 2-D GISAXS patterns were collected by a 2-D area detector (Pilatus, 7 ms per frame, 169 mm by 179 mm) with a sample-to-detector distance of 511 cm. The 1-D GISAXS profiles were obtained by reducing the 2-D patterns along the in-plane direction with background subtraction according to the sample film transmission, *i.e.* the ratio of the specular beam intensities between sample on substrate and pure substrate in the identical GISAXS geometry. The TEM samples were prepared by utilizing focused ion beam (FEI Helios 600i) slicing vertically along the solar cell device. The samples had thickness <100 nm. The TEM images were obtained on a FEI Tecnai G2 T20 microscope operating at 200 keV. The meso-scaled morphologies were observed by SEM (JEOL JSM-6500F). The powder XRD was performed on a X-ray diffractometer (PANalytical X'Pert PRO) irradiated with Cu Kα (wavelength = 1.54 Å). The topographic observation was analysed by AFM (Digital Instruments, Nanoscopes III).

ToF-SIMS measurements

The TOF-SIMS was performed with a PHI TRIFT V nanoTOF (Chigasaki, Japan) ToF-SIMS system. The pulsed primary ion source was Bi^+ and was operated at 30 kV (1 nA DC) with a 50 μm × 50 μm rastering area (256 × 256 scattered pixels with ~200 nm beam size) at an incident angle of 40°. The pulse width was about 10 ns and the *m*/*z* of the primary beam was selected using a double pulser system. The pulse rate is 7950 Hz and the acquisition dosage is $\sim 1.2 \times 10^{12}$ ion per cm^2. The analyzer collects positively charged secondary ions with a 240 eV pass-band from a direction that is normal to the specimen surface. The mass resolution of $[H_3COC_6H_4NCH_3]^+$ (136.0762) is ~7000 m/Δm. A 10 V pulsed flooding electron beam was used for charge compensation. The Ar cluster ion is generated by adiabatic expansion from 640 kPa. The depth profile is done by Wien-filtered Ar_{2500}^+ ion beam operated at 10 kV and 5 nA with a 1000 μm × 1000 μm rastering area at an incident angle of 40°.

Acknowledgements

Financial support obtained from Ministry of Science and Technology of Taiwan (Project 102-3113-P-002-027) and Institute of Nuclear Energy Research (Projects 103-S-A18) is highly appreciated.

Notes and references

1 P. Docampo, J. M. Ball, M. Darwich, G. E. Eperon and H. J. Snaith, *Nat. Commun.*, 2013, **4**, 2761.
2 J. Burschka, N. Pellet, S. J. Moon, R. Humphry-Baker, P. Gao, M. K. Nazeeruddin and M. Grätzel, *Nature*, 2013, **499**, 316–319.
3 I. Chung, B. Lee, J. He, R. P. Chang and M. G. Kanatzidis, *Nature*, 2012, **485**, 486–489.
4 M. Liu, M. B. Johnston and H. J. Snaith, *Nature*, 2013, **501**, 395–398.
5 J. H. Heo, S. H. Im, J. H. Noh, T. N. Mandal, C.-S. Lim, J. A. Chang, Y. H. Lee, H.-J. Kim, A. Sarkar, M. K. Nazeeruddin, M. Grätzel and S. I. Seok, *Nat. Photonics*, 2013, **7**, 486–491.
6 D. Liu and T. L. Kelly, *Nat. Photonics*, 2013, **8**, 133–138.
7 H. S. Kim, C. R. Lee, J. H. Im, K. B. Lee, T. Moehl, A. Marchioro, S. J. Moon, R. Humphry-Baker, J. H. Yum, J. E. Moser, M. Grätzel and N. G. Park, *Sci. Rep.*, 2012, **2**, 591.
8 M. M. Lee, J. Teuscher, T. Miyasaka, T. N. Murakami and H. J. Snaith, *Science*, 2012, **338**, 643–647.
9 H. Zhou, Q. Chen, G. Li, S. Luo, T. B. Song, H. S. Duan, Z. Hong, J. You, Y. Liu and Y. Yang, *Science*, 2014, **345**, 542–546.
10 J. H. Im, I. H. Jang, N. Pellet, M. Grätzel and N. G. Park, *Nat. Nanotechnol.*, 2014, **9**, 927–932.
11 N. J. Jeon, J. H. Noh, Y. C. Kim, W. S. Yang, S. Ryu and S. I. Seok, *Nat. Mater.*, 2014, **13**, 897–903.
12 J. B. You, Z. R. Hong, Y. Yang, Q. Chen, M. Cai, T. B. Song, C. C. Chen, S. R. Lu, Y. S. Liu, H. P. Zhou and Y. Yang, *ACS Nano*, 2014, **8**, 1674–1680.
13 G. E. Eperon, V. M. Burlakov, A. Goriely and H. J. Snaith, *ACS Nano*, 2014, **8**, 591–598.

14 K. W. Tan, D. T. Moore, M. Saliba, H. Sai, L. A. Estroff, T. Hanrath, H. J. Snaith and U. Wiesner, *ACS Nano*, 2014, **8**, 4730–4739.
15 S. Kazim, M. K. Nazeeruddin, M. Grätzel and S. Ahmad, *Angew. Chem., Int. Ed.*, 2014, **53**, 2812–2824.
16 H. J. Snaith, *J. Phys. Chem. Lett.*, 2013, **4**, 3623–3630.
17 H. S. Jung and N. G. Park, *Small*, 2015, **11**, 10–25.
18 J. You, L. Dou, K. Yoshimura, T. Kato, K. Ohya, T. Moriarty, K. Emery, C. C. Chen, J. Gao, G. Li and Y. Yang, *Nat. Commun.*, 2013, **4**, 1446.
19 A. Yella, H. W. Lee, H. N. Tsao, C. Yi, A. K. Chandiran, M. K. Nazeeruddin, E. W. Diau, C. Y. Yeh, S. M. Zakeeruddin and M. Grätzel, *Science*, 2011, **334**, 629–634.
20 M. A. Green, K. Emery, Y. Hishikawa, W. Warta and E. D. Dunlop, *Prog. Photovoltaics*, 2015, **23**, 1–9.
21 P. Qin, S. Paek, M. I. Dar, N. Pellet, J. Ko, M. Grätzel and M. K. Nazeeruddin, *J. Am. Chem. Soc.*, 2014, **136**, 8516–8519.
22 D. Nanova, A. K. Kast, M. Pfannmoller, C. Muller, L. Veith, I. Wacker, M. Agari, W. Hermes, P. Erk, W. Kowalsky, R. R. Schroder and R. Lovrincic, *Nano Lett.*, 2014, **14**, 2735–2740.
23 Z. L. Zhu, Y. Bai, T. Zhang, Z. K. Liu, X. Long, Z. H. Wei, Z. L. Wang, L. X. Zhang, J. N. Wang, F. Yan and S. H. Yang, *Angew. Chem., Int. Ed.*, 2014, **53**, 12571–12575.
24 Y. Shao, Z. Xiao, C. Bi, Y. Yuan and J. Huang, *Nat. Commun.*, 2014, **5**, 5784.
25 C.-H. Chiang, Z.-L. Tseng and C.-G. Wu, *J. Mater. Chem. A*, 2014, **2**, 15897–15903.
26 A. T. Barrows, A. J. Pearson, C. K. Kwak, A. D. F. Dunbar, A. R. Buckley and D. G. Lidzey, *Energy Environ. Sci.*, 2014, **7**, 2944.
27 D. Zhao, M. Sexton, H.-Y. Park, G. Baure, J. C. Nino and F. So, *Adv. Energy Mater.*, 2015, **5**, 1401855.
28 J. Y. Jeng, K. C. Chen, T. Y. Chiang, P. Y. Lin, T. D. Tsai, Y. C. Chang, T. F. Guo, P. Chen, T. C. Wen and Y. J. Hsu, *Adv. Mater.*, 2014, **26**, 4107–4113.
29 J. H. Kim, P. W. Liang, S. T. Williams, N. Cho, C. C. Chueh, M. S. Glaz, D. S. Ginger and A. K. Jen, *Adv. Mater.*, 2014, **27**, 695–701.
30 W. Nie, H. Tsai, R. Asadpour, J.-C. Blancon, A. J. Neukirch, G. Gupta, J. J. Crochet, M. Chhowalla, S. Tretiak, M. A. Alam, H.-L. Wang and A. D. Mohite, *Science*, 2015, **347**, 522–525.
31 H. Zhou, Q. Chen, G. Li, S. Luo, T. B. Song, H. S. Duan, Z. Hong, J. You, Y. Liu and Y. Yang, *Science*, 2014, **345**, 542–546.
32 M. Xiao, F. Huang, W. Huang, Y. Dkhissi, Y. Zhu, J. Etheridge, A. Gray-Weale, U. Bach, Y. B. Cheng and L. Spiccia, *Angew. Chem., Int. Ed.*, 2014, **53**, 9898–9903.
33 G. E. Eperon, V. M. Burlakov, P. Docampo, A. Goriely and H. J. Snaith, *Adv. Funct.Mater.*, 2014, **24**, 151–157.
34 Q. Chen, H. Zhou, Z. Hong, S. Luo, H. S. Duan, H. H. Wang, Y. Liu, G. Li and Y. Yang, *J. Am. Chem. Soc.*, 2014, **136**, 622–625.
35 S. D. Stranks, G. E. Eperon, G. Grancini, C. Menelaou, M. J. Alcocer, T. Leijtens, L. M. Herz, A. Petrozza and H. J. Snaith, *Science*, 2013, **342**, 341–344.
36 C. Wehrenfennig, G. E. Eperon, M. B. Johnston, H. J. Snaith and L. M. Herz, *Adv. Mater.*, 2014, **26**, 1584–1589.
37 T. C. Sum and N. Mathews, *Energy Environ. Sci.*, 2014, **7**, 2518–2534.
38 E. L. Unger, E. T. Hoke, C. D. Bailie, W. H. Nguyen, A. R. Bowring, T. Heumüller, M. G. Christoforo and M. D. McGehee, *Energy Environ. Sci.*, 2014, **7**, 3690–3698.
39 N. J. Jeon, J. H. Noh, Y. C. Kim, W. S. Yang, S. Ryu and S. I. Seol, *Nat. Mater.*, 2014, **13**, 897–903.
40 M. D. McGehee, *Nat. Mater.*, 2014, **13**, 845–846.
41 K. Wojciechowski, S. D. Stranks, A. Abate, G. Sadoughi, A. Sadhanala, N. Kopidakis, G. Rumbles, C. Z. Li, R. H. Friend, A. K. Y. Jen and H. J. Snaith, *ACS Nano*, 2014, **8**, 12701–12709.
42 H. C. Liao, C. S. Tsao, T. H. Lin, M. H. Jao, C. M. Chuang, S. Y. Chang, Y. C. Huang, Y. T. Shao, C. Y. Chen, C. J. Su, U. S. Jeng, Y. F. Chen and W. F. Su, *ACS Nano*, 2012, **6**, 1657–1666.
43 H. C. Liao, C. S. Tsao, T. H. Lin, C. M. Chuang, C. Y. Chen, U. S. Jeng, C. H. Su, Y. F. Chen and W. F. Su, *J. Am. Chem. Soc.*, 2011, **133**, 13064–13073.
44 H.-C. Liao, C.-S. Tsao, Y.-T. Shao, S.-Y. Chang, Y.-C. Huang, C.-M. Chuang, T.-H. Lin, C.-Y. Chen, C.-J. Su, U. S. Jeng, Y.-F. Chen and W.-F. Su, *Energy Environ. Sci.*, 2013, **6**, 1938.
45 J. H. Im, C. R. Lee, J. W. Lee, S. W. Park and N. G. Park, *Nanoscale*, 2011, **3**, 4088–4093.
46 A. Kojima, K. Teshima, Y. Shirai and T. Miyasaka, *J. Am. Chem. Soc.*, 2009, **131**, 6050–6051.
47 J. M. Ball, S. D. Stranks, M. T. Hörantner, S. Hüttner, W. Zhang, E. J. W. Crossland, I. Ramirez, M. Riede, M. B. Johnston, R. H. Friend and H. J. Snaith, *Energy Environ. Sci.*, 2015, **8**, 602–609.
48 G. Renaud, R. Lazzari and F. Leroy, *Surf. Sci. Rep.*, 2009, **64**, 255–380.
49 T. R. Andersen, T. T. Larsen-Olsen, B. Andreasen, A. P. L. Bottiger, J. E. Carle, M. Helgesen, E. Bundgaard, K. Norrman, J. W. Andreasen, M. Jorgensen and F. C. Krebs, *ACS Nano*, 2011, **5**, 4188–4196.
50 C. Y. Chen, C. S. Tsao, Y. C. Huang, H. W. Liu, W. Y. Chiu, C. M. Chuang, U. S. Jeng, C. J. Su, W. R. Wu, W. F. Su and L. Wang, *Nanoscale*, 2013, **5**, 7629–7638.
51 S. R. Kline, *J. Appl. Crystallogr.*, 2006, **39**, 895–900.
52 J. Teixeira, *J. Appl. Crystallogr.*, 1988, **21**, 781–785.
53 S. H. Chen and J. Teixeira, *Phys. Rev. Lett.*, 1986, **57**, 2583–2586.
54 G. Laudisio, R. K. Dash, J. P. Singer, G. Yushin, Y. Gogotsi and J. E. Fischer, *Langmuir*, 2006, **22**, 8945–8950.
55 E. Edri, S. Kirmayer, A. Henning, S. Mukhopadhyay, K. Gartsman, Y. Rosenwaks, G. Hodes and D. Cahen, *Nano Lett.*, 2014, **14**, 1000–1004.
56 E. Edri, S. Kirmayer, S. Mukhopadhyay, K. Gartsman, G. Hodes and D. Cahen, *Nat. Commun.*, 2014, **5**, 3461.
57 S. Aharon, B. E. Cohen and L. Etgar, *J. Phys. Chem. C*, 2014, **118**, 17160–17165.

58 L. Etgar, P. Gao, Z. Xue, Q. Peng, A. K. Chandiran, B. Liu, M. K. Nazeeruddin and M. Grätzel, *J. Am. Chem. Soc.*, 2012, **134**, 17396–17399.
59 J. Shi, J. Dong, S. Lv, Y. Xu, L. Zhu, J. Xiao, X. Xu, H. Wu, D. Li, Y. Luo and Q. Meng, *Appl. Phys. Lett.*, 2014, **104**, 063901.
60 W. A. Laban and L. Etgar, *Energy Environ. Sci.*, 2013, **6**, 3249.
61 A. Y. Mei, X. Li, L. F. Liu, Z. L. Ku, T. F. Liu, Y. G. Rong, M. Xu, M. Hu, J. Z. Chen, Y. Yang, M. Grätzel and H. W. Han, *Science*, 2014, **345**, 295–298.